Journal of Laser Applications

RESEARCH ARTICLE | SEPTEMBER 11 2023

# Experimental and numerical study on grain refinement in electromagnetic assisted laser beam welding of 5754 Al alloy

**Special Collection:** Proceedings of the International Congress of Applications of Lasers & Electro-Optics (ICALEO 2023)

Chunliang Yang ; Fan Yang ; Xiangmeng Meng ; Stephen Nugraha Putra ; Marcel Bachmann ; Michael Rethmeier



*J. Laser Appl.* 35, 042007 (2023)
https://doi.org/10.2351/7.0001085

Journal of Laser Applications ARTICLE pubs.aip.org/lia/jla

# Experimental and numerical study on grain refinement in electromagnetic assisted laser beam welding of 5754 Al alloy

Cite as: J. Laser Appl. 35, 042007 (2023); doi: 10.2351/7.0001085
Submitted: 20 June 2023 · Accepted: 22 August 2023 ·
Published Online: 11 September 2023



Chunliang Yang,[1] Fan Yang,[1] Xiangmeng Meng,[1] Stephen Nugraha Putra,[1] Marcel Bachmann,[1] and Michael Rethmeier[1,2,3]

## AFFILIATIONS

[1]Bundesanstalt für Materialforschung und -prüfung (BAM), Unter den Eichen 87, 12205 Berlin, Germany
[2]Technische Universität Berlin, Pascalstraße 8-9, 10587 Berlin, Germany
[3]Fraunhofer Institute for Production Systems and Design Technology, Pascalstraße 8-9, 10587 Berlin, Germany

**Note:** Paper published as part of the special topic on Proceedings of the International Congress of Applications of Lasers & Electro-Optics 2023.

## ABSTRACT

Through experimental observation and auxiliary numerical simulation, this investigation studies the different types of grain refinement of 5754 aluminum alloy laser beam welding by applying a transverse oscillating magnetic field. Scanning electron microscope results have proved that the application of a magnetic field can reduce the average crystal branch width and increase its number. The interaction between the induced eddy current generated by the Seebeck effect and the applied external magnetic field produces a Lorentz force, which is important for the increase in the number of crystal branches. Based on the theory of dendrite fragmentation and the magnetic field-induced branches increment, the grain size reduction caused by the magnetic field is studied. Furthermore, the effects of the magnetic field are analyzed by combining a phase field method model and simulations of nucleation and grain growth. The grain distribution and average grain size after welding verify the reliability of the model. In addition, the introduction of a magnetic field can increase the number of periodic three-dimensional solidification patterns. In the intersection of two periods of solidification patterns, the metal can be re-melted and then re-solidified, which prevents the grains, that have been solidified and formed previously, from further growth and generates some small cellular grains in the new fusion line. The magnetic field increases the building frequency of these solidification structures and thus promotes this kind of grain refinement.

Key words: laser beam welding, magnetic field, crystal branch development, grain refinement, periodic solidification pattern





## I. INTRODUCTION

One of the most promising metal joining technologies is laser beam welding (LBW), which is widely employed in industries, such as aerospace, shipbuilding, automobiles, and pressure vessels.[1] Good penetration capacity, high attainable welding speed, limited heat-affected zone, and low welding distortion are key advantages of LBW. However, LBW still meets several challenges, including porosity, molten pool collapses, humping defects in high-speed welding, heterogeneous mixing with filler wire, and insufficient fine grains, making it difficult to realize the benefits mentioned above. Particularly, the molten pool will inevitably experience high temperatures, causing the grains to become coarse because the grain boundary mobility is controlled by temperature. At high temperatures, grain boundary mobility is high, and grains are coarsened,[2] reducing the mechanical properties and service performance of the joint. The grain structure of a weld has a high influence on the strength and ductility of the joint[3] and on the susceptibility of the weld to the formation of hot cracks.[4] Small grains will lead to many grain boundaries. Therefore, the mechanical load that may have occurred during the material curing process is dispersed,

which reduces the hot cracking risk.[4] A large number of grain boundaries will also increase the strength of the material.[3]

Many laser welding modification procedures have been developed to obtain better grain distribution, refine the grains, and increase the mechanical properties of joints, such as oscillation laser welding[5] and pulsed laser welding.[6] Among them, electromagnetic stirring LBW (EMS-LBW) is considered one of the most promising optimization processes for LBW.

There have been studies indicating that a magnetic field has many benefits for LBW, including preventing root collapse[7] and improving weld morphology.[8] It can also stir the molten pool, promoting material flow[9] and stabilizing the keyhole to reduce porosity.[10] Additionally, it can promote the uniform distribution of added elements,[11] improve plasma distribution,[12] enhance surface roughness,[13] and improve the distribution of residual stress after welding.[14] Moreover, the magnetic field can refine grains and optimize their distribution,[15–20] which ultimately enhances the mechanical properties and usability of the joint.

Chen *et al.*[15] found that the prior-austenite grain size in the weld with an external magnetic field is more than two times smaller than those in the conventional LBW. In the results of Li *et al.*,[16] dendrites and cellular crystals near the weld center disappeared, and the grain size was refined. The experiments of Hu *et al.*[17] also show that the microstructure transforms from bulky banded and spherical structures to fine blocky and granular structures in the fusion zone, which leads to grain refinement. In the process of Xu *et al.*,[18] the electromagnetic field refines the grains and reduces the width of the columnar grain region to a certain extent. However, the magnetic field made the austenitic grains in the columnar grain zone refine, but these kinds of grains in the central region coarsen and even grow discontinuously in the interface zone.[19] The grain refinement was also observed by Meng *et al.*[20] in the upper part of the weld, while the grain became coarse in the lower part of the weld. They believe that the obvious reduction of grain size in the upper part of the weld is caused by dendrite fragmentation.

However, for various kinds of grains or grains in diverse zones, the role of magnetic field refinement in laser welding may be distinct. Also, the varied magnetic field parameters have different effects on microstructure evolution in LBW. It is necessary to classify and study magnetic field-induced grain refinement in detail.

In this work, the effect of a transverse alternating current magnetic field on the grain refinement of 5754 aluminum alloy laser beam welding was observed and investigated. The refinement effect of a magnetic field on crystal branches was studied by a scanning electron microscope (SEM) and analyzed by combining the Seebeck effect. Built upon the theory of dendrite fragmentation, the reduction of equiaxed grain size caused by the magnetic field is studied. Based on the phase field method (PFM) and nucleation theory, the nucleation and grain growth of equiaxed crystals are simulated, and the reliability of the model is verified by the average grain size after welding. The role of the magnetic field in the nucleation and grain growth of equiaxed crystals is studied. The distribution of grains in different directions on a larger area was then observed by a microscope, and it was found that the introduction of a magnetic field could increase the number of periodic solidification patterns, thus further refining the grains.

**TABLE I.** Physical parameters used in the experiment and simulation.

| Parameters | Values |
|---|---|
| Focal length | 350 mm |
| Spot diameter | 0.56 mm |
| Wavelength | 1070 nm |
| Laser power | 4 kW |
| Welding speed | 3 m/min |
| Magnet poles position | 2 mm above the workpiece |
| Magnet poles spacing | 15 mm |
| Magnet frequency | 3300 Hz |
| Max RMS magnetic flux density | 300 mT |

## II. EXPERIMENT

Bead-on-plate LBW was carried out on the AA5754 aluminum alloy plate with a dimension of $300 \times 100 \times 10\,\text{mm}^3$. The relevant parameters of IPG YLR 20000 and in-house electromagnetic equipment as well as welding parameters are listed in Table I.

After welding, the grain distributions at the top surface and the longitudinal cross sections at the weld centerline were etched for 30 s using 20% tetrafluoroboric acid in water at 30 V, 25 °C, and observed with a microscope. The longitudinal cross sections were then electropolished with Struers A2 reagent for 12 s at 39 V, 20 °C. The small equiaxed grains close to the fusion line were observed using the electron backscatter diffraction (EBSD) technology, and the crystal branch distribution was obtained using the SEM technology. However, these measurement methods are applied to the welded joints. Although some methods have been developed for real-time observation, they are not suitable for the welding process. To analyze the processing more deeply, it is necessary to combine it with simulation methods.

## III. MODELING METHODOLOGY

For further study about the fragmentation-induced grain refinement of equiaxed grain, a simple PFM model was set up to analyze this dynamic process of equiaxed grain.

The model is a two-dimensional model of $512 \times 512\,(\text{grid cells})^2$, and the unit length $dx = dy = 0.293\,\mu\text{m}$, that is, $150 \times 150\,\mu\text{m}^2$. The time step is $1\,\mu\text{s}$. The thermal cycle used in the PFM model is obtained by the macro computational fluid dynamics model,[21] and it is fitted as a quadratic function with time. Equation (1) is used to update the temperature with time in PFM calculation. Here, only the temperature change with time is considered, and the initial temperature is the liquidus temperature of 910 K,

$$T = 910 - 3491t + 10\,978t^2, \tag{1}$$

where $t$ is the time.

Every grain can be regarded as a field, if the order parameter $\eta_p = 1$, it is within the grain with number $p$, if $\eta_p = 0$, it is outside the grain $p$, and if $0 \text{lt} \eta_p < 1$, it is at the boundary of the grain $p$. When the order parameter of each field at a certain position is 0, the position is the liquid phase, and the initial condition is the liquid phase everywhere.

For conventional LBW, the relationship between nucleation density increment and supercooling can be described by the continuous nucleation model proposed by Thévoz *et al.*,[22]

$$\frac{dn}{d(\Delta T)} = \frac{n_{\max}}{\sqrt{2\pi}(\Delta T_\sigma)} \exp\left[-\frac{1}{2}\left(\frac{\Delta T - \Delta T_N}{\Delta T_\sigma}\right)^2\right], \quad (2)$$

where $\Delta T = T_l - T$ is the supercooling degree, $n_{\max} = 6 \times 10^{15}\ \mathrm{m}^{-3}$ is the maximum nucleation density, and $\Delta T_N = 5.0\ \mathrm{K}$ and $\Delta T_\sigma = 0.5\ \mathrm{K}$ are the average and standard deviation of the supercooling degree, respectively.[23]

When a magnetic field is applied, as shown in Fig. 1, for an equiaxed crystal with nucleation and growth, there are four primary dendrites and several secondary dendrites on eight sides. Assuming that three secondary dendrites on each side are independent enough, one crystal nucleus will produce at most 28 new crystal nuclei when dendrites are fragmented. Considering there are more branches with a magnetic field, the ratio between the branches number in unit length with and without magnetic field got from experiment results in the result and discussion part (Fig. 2) was also introduced (14/9), and a fragmentation number coefficient $n_b$ can be driven,

$$n_b = \frac{14}{9}(4 + 8 \times 3). \quad (3)$$

The relationship between the nucleation density increments of the newly formed crystal nucleus and the supercooling degree, when fragmentation occurs, can be expressed as follows:

$$\frac{dn}{d(\Delta T)} = \frac{n_b n_{\max}}{\sqrt{2\pi}(\Delta T_\sigma)} \exp\left[-\frac{1}{2}\left(\frac{\Delta T - \Delta T_N}{\Delta T_\sigma}\right)^2\right]. \quad (4)$$

By integrating Eq. (2) or Eq. (4) and accumulating them in grids, the nucleation rates under different conditions can be obtained,

$$P_n = V_{\mathrm{cell}} \int_{\Delta T}^{\Delta T + \delta(\Delta T)} \frac{dn}{d(\Delta T')} \delta(\Delta T'), \quad (5)$$

where $\Delta T'$ represents the variable of subcooling degree. Furthermore, the nucleation probability $P_n$ can be obtained, where $V_{cell}$ is the cell volume. Since the model here is two-dimensional, it is assumed that the thickness direction is also a cell thickness.

For conventional LBW, a random number of 0–1 is given to the grid at each time step. When the random number is greater than $P_n$, the grid with a radius of $2dx$ is set as a new crystal nucleus with a field number of 1–36 in the liquid.

For the case with a magnetic field, considering that dendrite fragmentation will only occur when the initially formed crystal nuclei have branches, it is assumed that the nucleation rate is calculated by Eq. (2) before 1.5 ms and the new nuclear with a radius of $2dx$ in the liquid, and after 1.5 ms, it is calculated by Eq. (4) with a radius of $7dx$ in the liquid or at the boundary of the existed grains. The size of the nucleus formed by fragmentation is estimated by the dendrite morphology of a binary alloy solidification PFM model growth starts from a nucleus.

In addition to nucleation, grains will also grow. For simplicity, the phase field method was used, without considering the crystal branches caused by anisotropy. The variation of phase field order parameters with time can be obtained by the following equation:[24]

$$\frac{d\eta_p}{dt} = -L\left[-A_1\eta_p + A_1\eta_p^3 + K_1\eta_p \sum_{q \neq p}^{n} \eta_q^3 - \frac{W_\phi^2}{\tau}(\nabla\eta_p)^2\right], \quad (6)$$

where $\eta_p$ is the phase field order parameter corresponding to grain $p$; $t$ is the time; and $L$ is the interface mobility, which is described by Eq. (7);[2] $A_2 = 1.4 \times 10^6$ is the coefficient of the constructed double-well potential function; $K_1 = 2.9 \times 10^7\ \mathrm{s}^{-1}$ is the parameter related to the grain boundary action range; $\eta_q$ is the order parameter with the number of other grains except for the $p$; $W_\phi^2$ is the square of the interface characteristic length; $\tau$ is the characteristic relaxation time; and the value of $\frac{W_\phi^2}{\tau}$ is$2.57 \times 10^{-7}\ \mathrm{m}^2/\mathrm{s}$,

$$L = \frac{\pi^2}{8\delta}\frac{M_0}{T}\exp\left(-\frac{Q_b}{RT}\right), \quad (7)$$

where $\delta = 1.2\,\mu\mathrm{m}$ is the interface thickness, $M_0 = 0.811\,94\ \mathrm{m}^4\mathrm{K/J\,s}$ $\frac{-b+\sqrt{b^2-4ac}}{2a}$ is the fitted parameter, $Q_b = 89\,375\ \mathrm{J/mol}$ is the activation energy,[25] and $R = 8.314\ \mathrm{J\,mol}^{-1}\ \mathrm{K}^{-1}$ is the gas constant.

The simulated time is 50 ms. At that time, the temperature reaches 763 K. Since the subsequent grain growth is relatively slow, it can be ignored.

According to the nucleation and growth of the phase field, a simple phase field model can be established, which only includes nucleation and grain growth.

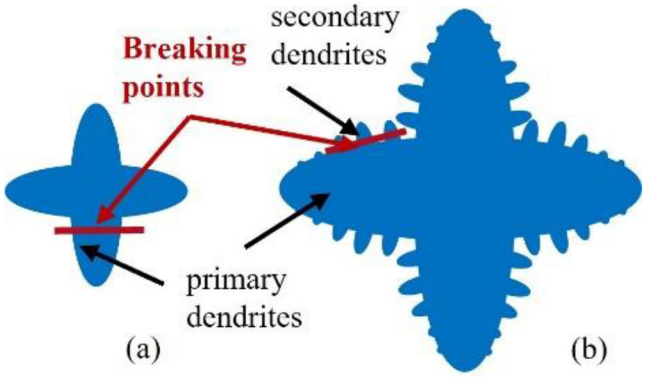


**FIG. 1.** The schematic diagram of dendrite fragmentation of (a) primary dendrites and (b) secondary dendrites for equiaxed crystal.

## IV. RESULT AND DISCUSSION

The crystal branches of the equiaxed crystal near the fusion line at the bottom of the molten pool were scanned by SEM, as

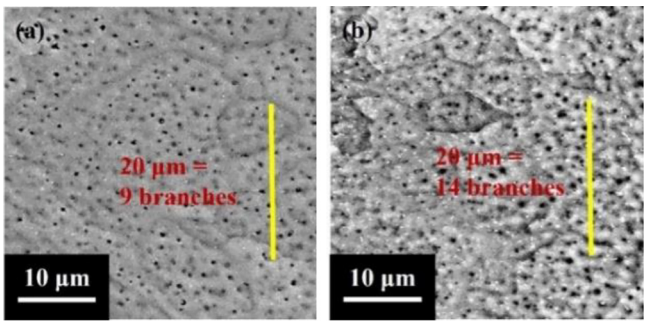


FIG. 2. The crystal branch distribution (a) without a magnetic field and (b) with a magnetic field.

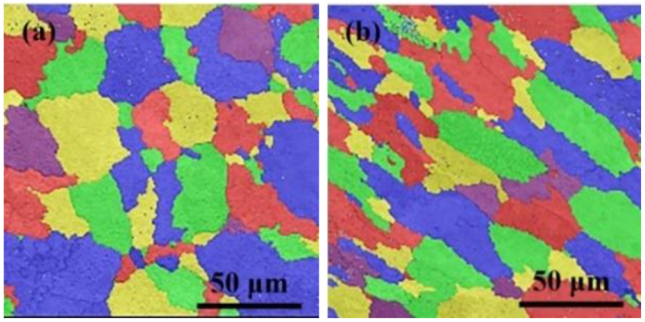


FIG. 4. The grains distribution near the fusion line at the longitudinal cross section at the weld centerline (a) without the magnetic field and (b) with the magnetic field.

shown in Fig. 2, and the schematic diagram of the scanning position is shown in Fig. 3. The average branch width is 2.22 $\mu$m/branch without a magnetic field, while it is 1.42 $\mu$m/branch with a magnetic field. After the magnetic field is applied, the number of branches increases (36%), which leads to the competition and mutual inhibition of branches; thus, the branch widths decrease.

The electromagnetic field will generate two kinds of Lorentz force. One comes from the interaction between the magnetic field with the current generated from conductive liquid metal flows in a magnetic field. Due to the temperature gradient at the solidification interface of the molten pool, there will be an electric field at the solidification interface under the action of the magnetic field according to the Seebeck effect. When the generated electric field interacts with the applied magnetic field, another kind named thermal electromagnetic Lorentz force is produced, which is stronger than the former one near the solidification interface.[26] The thermal electromagnetic Lorentz force will affect the flow and then the concentration and free energy distribution, thus further promoting the formation of branches.

The refinement of crystal branches makes the substructure inside the grain finer, which is beneficial for improving the mechanical properties of the joint. At the same time, it also

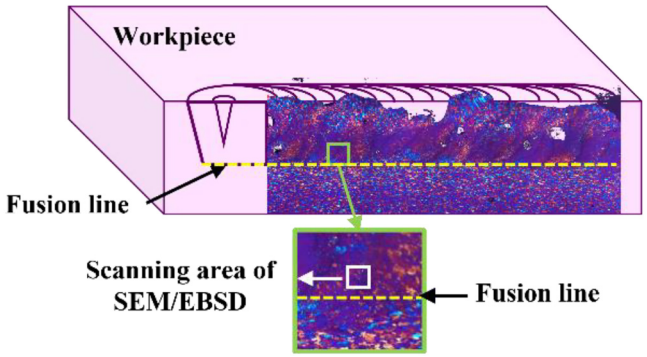


FIG. 3. The schematic diagram of the scanning position of SEM/EBSD.

provides more opportunities for dendrite fragmentation. In the study of Al–Cu alloy by Cao *et al.*,[27] the promotion of magnetic field on branching in dendrite area was also found. The promotion of a magnetic field on branching is different in different alloys and different grain regions; in general, a magnetic field will promote branching.

The EBSD results of the longitudinal cross sections near the bottom fusion line are shown in Fig. 4, and the schematic diagram of the scanning position is shown in Fig. 3. To calculate the average grain size, one needs the number of grains in the selected area. The average grain area is equal to the area size divided by the number of counted grains. By assuming that the grain is a circle, the average grain size, which is the diameter of the circle, can be calculated accordingly. The average grain size is 29.5 $\mu$m without a magnetic field, while it is 23.9 $\mu$m with a magnetic field. After the magnetic field is applied, the average grain size decreases. The grain size is reduced by 19%. For the grain refinement when the magnetic field is applied, the extra nucleation rate caused by dendrite fragmentation is considered the main reason.[20] To study the influence of magnetic field on grain size and fragmentation-induced grain refinement, the results of the PFM model are needed.

The calculation results of several characteristic time points during nucleation and at the end of the calculation are extracted and analyzed. Figure 5 shows the distribution of the sum of the phase field order parameters that vary with time without a magnetic field. If the sum of the phase field order parameters is 1, it means solid and 0 means liquid. When the supercooling reaches a certain level, crystal nuclei are generated one after another, as shown in Fig. 5(a). Owing to the different appearance times, some crystal nuclei have grown up and some are very small. When the temperature continues to drop, there will no new crystal nucleus exists [Fig. 5(b)]. However, due to the influence of boundary migration, the crystal nucleus growth and the liquid phase will gradually disappear, and no new crystal nucleus will be produced during the grain growth process. When two grains grow until they encounter each other, they will compete again themselves [Figs. 5(b)–5(e)] until the liquid phase disappears [Figs. 5(e) and 5(f)].

The grain evolution after applying the magnetic field is shown in Fig. 6. In the initial stage, crystal nuclei are also generated and

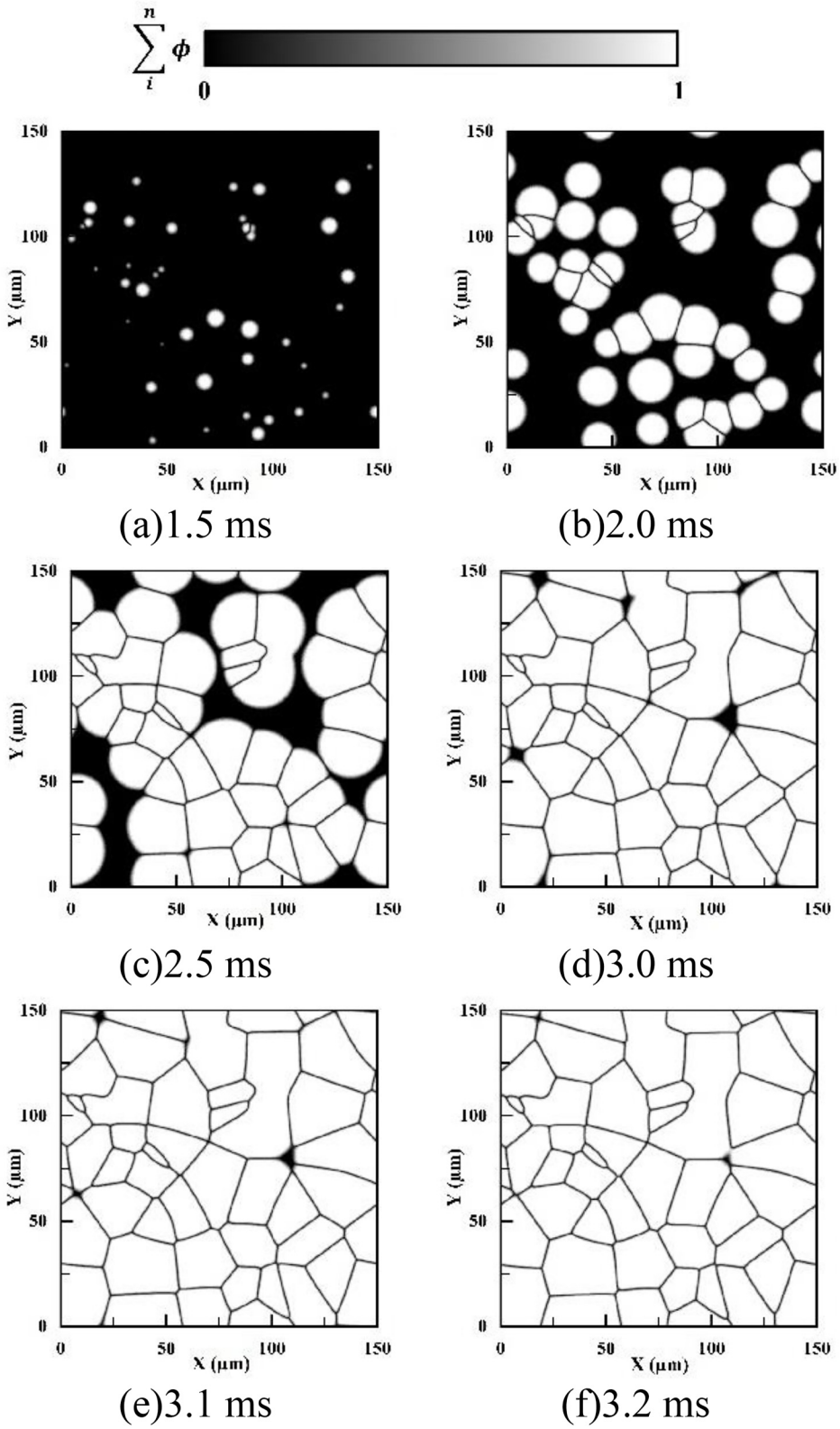


**FIG. 5.** The grains distribution varies with time in the solidification stage without a magnetic field. (a) 1.5, (b) 2.0, (c) 2.5, (d) 3.0, (e) 3.1, and (f) 3.2 ms.

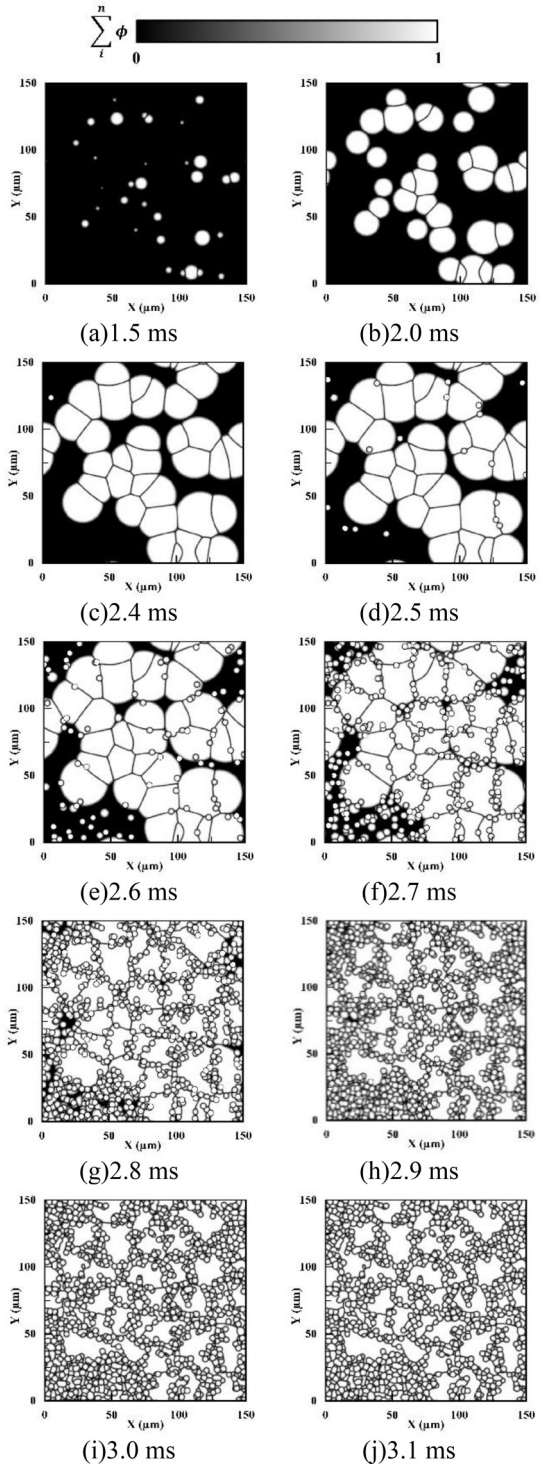


**FIG. 6.** The grains distribution varies with time in the solidification stage with a magnetic field. (a) 1.5, (b) 2.0, (c) 2.4, (d) 2.5, (e) 2.6, (f) 2.7, (g) 2.8, (h) 2.9, (i) 3.0, and (j) 3.1 ms.

grow up due to undercooling [Figs. 6(a) and 6(b)]. When the grain grows to a certain extent, the crystal nucleus generated by dendrite fragmentation calculated by Eq. (4) begins to appear [Fig. 6(c)]. These grains may have just separated from the original grains and, thus, it can be assumed that the grains are set at the boundary of the existing grains, or they may have fallen off, so it can make another assumption that the grains are set to appear in the liquid area [Figs. 6(c)–6(h)]. When the liquid disappears, there is no difference in the Seebeck coefficient, so there will be no thermal current at the grain boundary, no thermoelectric Lorentz force and dendrite fragmentation, and no crystal nucleus generated by fragmentation [Figs. 6(h)–6(j)]. Interestingly, the time required for complete solidification is a few tenths milliseconds earlier than that without a magnetic field, which is caused by the continuous growth of the crystal nucleus produced by fragmentation. The fracture surface produces two opposite migrations of the grain boundary, which did not exist before, thus promoting the solidification.

The end of solidification does not mean the end of grain growth. At higher temperatures, the grain boundary mobility is still relatively large, so there will be competitive growth between adjacent grains, thus the grain size will further increase, as shown in Fig. 7. This figure shows the grains grow to (a) 10, (b) 2, (c) 30, (d) 40, and (e) 50 ms. Column (1) is the case where no magnetic field is applied, and column (2) shows the case when a magnetic field is applied. Compared with column (1), although the temperature change and the grain boundary mobility of column (2) are the same, there are many small grains in column (2), which leads to more intense competition, thus more grains disappear during the competition. However, additional crystal nuclei are produced when the magnetic field is applied, so the number of crystal grains is still higher, and the size is still smaller at the end of the calculation. At 50 ms, as shown in Fig. 7(e), the calculated average grain sizes are 28.6 and 22.6 $\mu$m, which are very close to the experimental results in Fig. 4 (29.5 and 23.9 $\mu$m); thus, the reliability of the model can be verified and the error does not exceed 6%. Obviously, with increasing time the difference between cases with and without magnetic field is getting smaller because many small grains are more likely to disappear by competition or be swallowed up by each other, so the change in this stage is relatively large.

In addition to the refinements induced by the increase and fragmentation of branches, a special situation that will also reduce the average size of grains has been found, that is, the periodic patterns of solidification of the molten pool.

The heat and force of the molten pool are unstable, and the backward hot fluid increases at a certain moment, which makes some dendrites that have been formed before melt again. This phenomenon can limit the size of these long dendrites. When the heat and force are a little smaller, fine cellular crystals and long dendrites will grow from the newly formed solid–liquid interface. In the region where the two periods are staggered, the dendrites or equiaxed crystals, that are already growing, will melt and then solidify again.[28] On the one hand, the long dendrites are fused, which limits the grain size. On the other hand, there are fine grains that are more beneficial to mechanical properties than the dendrites at each newly formed solidification interface.

This periodic solidification forms ripples that are reflected on the top surface,[29] so the top surface is a good object to be observed.

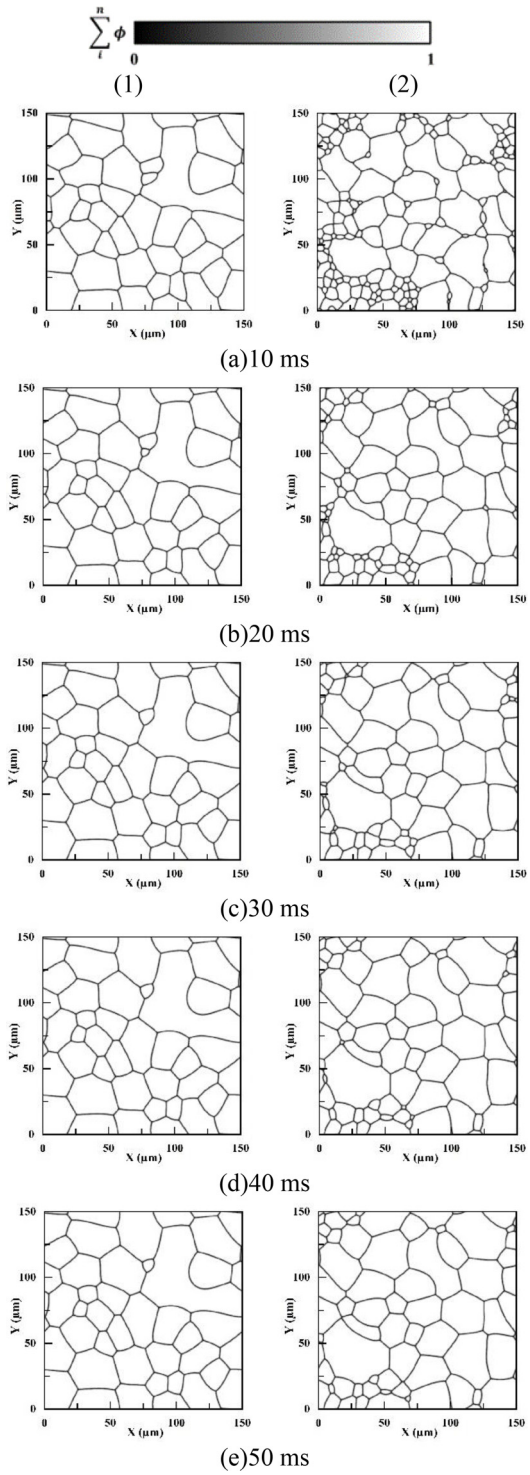


**FIG. 7.** The grains distribution varies with time after the solidification stage (1) without a magnetic field and (2) with a magnetic field. (a) 10, (b) 20, (c) 30, (d) 40, and (e) 50 ms.

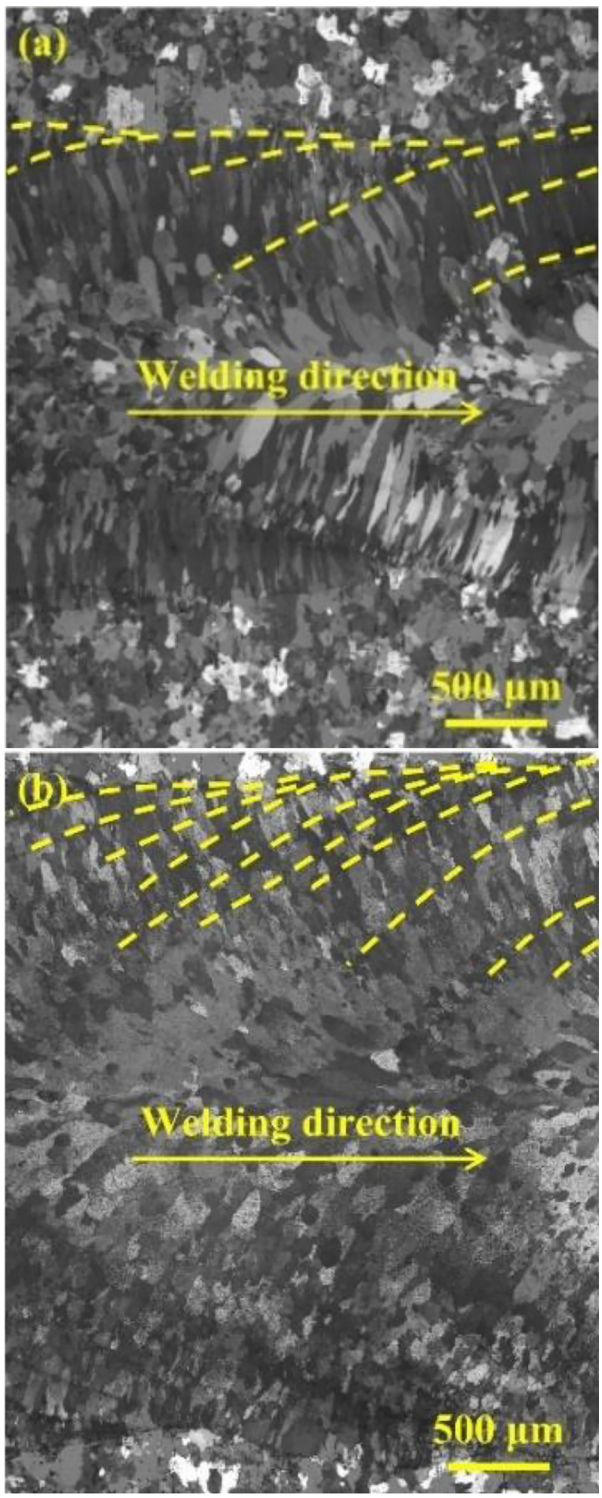


**FIG. 8.** The grains distribution at the top surface (a) without a magnetic field and (b) with a magnetic field.

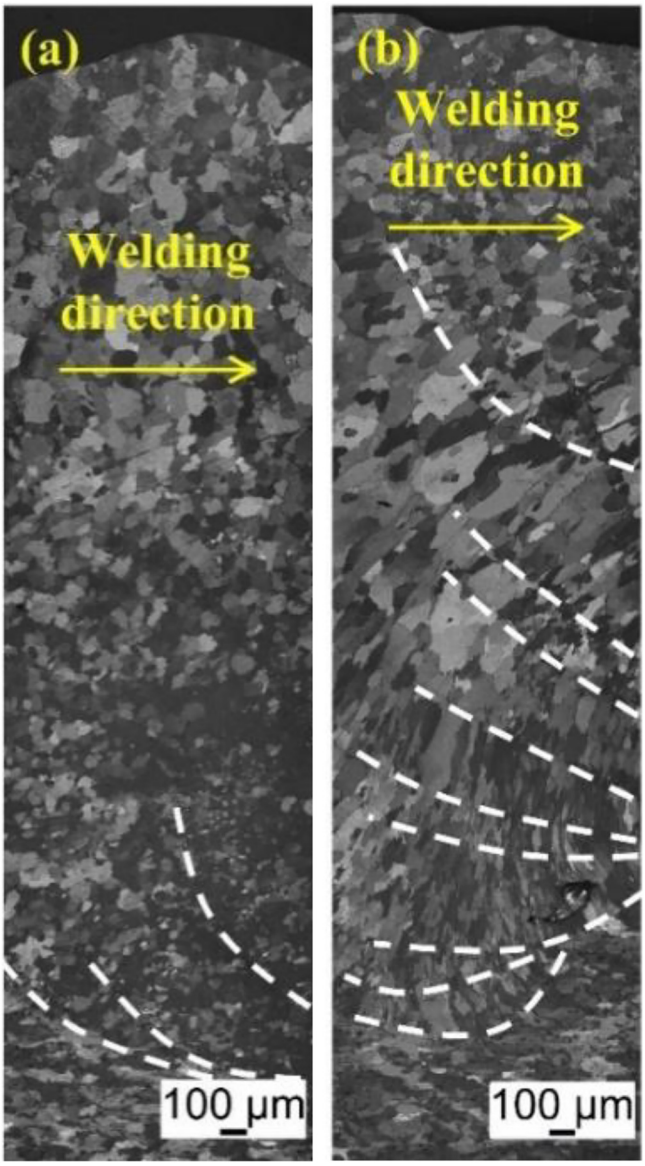


**FIG. 9.** The grains distribution in the longitudinal section at the weld centerline (a) without a magnetic field and (b) with a magnetic field.

As shown in Fig. 8, the grain distribution on the top surface without and with magnetic field, and the number of periodic solidification patterns in the same size area is counted and marked with yellow dotted lines. When the magnetic field is not applied, it is 6, but after the magnetic field is applied, it is 10. The magnetic field intensifies the grain refinement caused by periodic solidification. The electromagnetic Lorentz force circulates at the frequency of the magnetic field, which promotes the periodic change of molten pool oscillation, and then promotes the periodic solidification pattern.

The grain distributions in the longitudinal section at the weld centerline are also observed, as shown in Fig. 9, where the periodic solidification patterns are marked with white dotted lines. The number of cycles is 3 when no magnetic field is applied compared to 9 after the application of a magnetic field. The application of the magnetic field enhances the grain refinement by intensifying periodic solidification patterns.

This periodic solidification pattern seems related to ripples, and the influence of a magnetic field on the top surface waveform of gas tungsten arc weld was measured by Jeng *et al.*[30] The magnetic field makes the ripples on the top surface more and finer.

## V. CONCLUSIONS

The crystal branches refinement, equiaxed crystal grain refinement, and increment of grain refinement with periodic solidification patterns in laser beam welding caused by the magnetic field were observed using the microscope, SEM, and EBSD techniques. A PFM model was built to help to analyze the equiaxed crystal grain refinement.

1. The crystal branches of the equiaxed crystal near the fusion line at the bottom of the molten pool are scanned by SEM. After the magnetic field is applied, the number of crystal branches increases, and the branch widths decrease. The electric field generated by the Seebeck effect interacts with the applied magnetic field, and then the Lorentz force is produced, which promotes the formation of branches.
2. The EBSD results near the fusion line are analyzed. After the magnetic field is applied, the average grain size decreases.
3. Based on the phase field method and the nucleation rate considering the dendrites fragmentation, a phase field model was built and analyzed. The dendrite fragmentations bring extra nuclei after undercooling nucleation until solidification is over, leading to a smaller grain size when the magnetic field is applied.
4. The increment of the periodic solidification pattern by magnetic field was observed. This kind of periodic solidification pattern can fuse and limit the growth of long dendrites and produce more newly formed solidification interfaces with fine grains.

The assistance of magnetic field promotes the refinement of grain (19%) and subgrain (36%) structure in laser welding joints, which improves the quality of laser welding, especially the thick plate, and its application in aerospace, shipbuilding, automobile, pressure vessel, and other manufacturing industries.



## ACKNOWLEDGMENTS

The financial support from the Humboldt Research Fellowship for postdoctoral researchers, Deutsche Forschungsgemeinschaft (DFG, German Research Foundation, Project Nos. 506270597 and 466939224), and China Scholarship Council (No. 202008080270) is acknowledged.

## AUTHOR DECLARATIONS

### Conflict of Interest

The authors have no conflicts to disclose.

## Author Contributions

**Chunliang Yang:** Conceptualization (equal); Formal analysis (equal); Investigation (equal); Methodology (equal); Software (equal); Validation (equal); Visualization (equal); Writing – original draft (equal); Writing – review & editing (equal). **Fan Yang:** Methodology (equal); Software (equal); Validation (equal); Writing – review & editing (equal). **Xiangmeng Meng:** Methodology (equal); Software (equal); Validation (equal); Writing – review & editing (equal). **Stephen Nugraha Putra:** Methodology (equal); Software (equal); Validation (equal); Writing – review & editing (equal). **Marcel Bachmann:** Conceptualization (equal); Data curation (equal); Formal analysis (equal); Investigation (equal); Methodology (equal); Resources (equal); Software (equal); Supervision (equal); Writing – review & editing (equal). **Michael Rethmeier:** Conceptualization (equal); Data curation (equal); Project administration (equal); Resources (equal); Supervision (equal); Writing – review & editing (equal).

## REFERENCES


[1]H. Zhao, D. R. White, and T. DebRoy, "Current issues and problems in laser welding of automotive aluminium alloys," Int. Mater. Rev. **44**, 238–266 (1999).
[2]T. Takaki, T. Hirouchi, Y. Hisakuni, A. Yamanaka, and Y. Tomita, "Multi-phase-field model to simulate microstructure evolutions during dynamic recrystallization," Mater. Trans. **49**, 2559–2565 (2008).
[3]H. Fujita and T. Tabata, "The effect of grain size and deformation sub-structure on mechanical properties of polycrystalline aluminum," Acta Metall. **21**, 355–365 (1973).
[4]W. S. Pellini and W. R. Apblett, "Factors which influence weld hot cracking," Weld. Res. Suppl. **33**, 83–90 (1954).
[5]C. Hagenlocher, M. Sommer, F. Fetzer, R. Weber, and T. Graf, "Optimization of the solidification conditions by means of beam oscillation during laser beam welding of aluminum," Mater. Des. **160**, 1178–1185 (2018).
[6]N. Sommer, F. Stredak, M. Wiegand, and S. Böhm, "Grain growth and precipitation behaviour of AISI 430 ferritic stainless steel subjected to pulsed laser beam welding using free form pulse shaping," Weld. World **67**, 51–62 (2023).
[7]G. Ambrosy, P. Berger, H. Huegel, and D. Lindenau, "Improvement of laser beam welding by electromagnetic forces in the weld pool," Proc. SPIE **4831**, 175–179 (2003).
[8]X. Zhan, J. Zhou, W. Sun, J. Chen, and Y. Wei, "Effect of external applied steady magnetic field on the morphology of laser welding joint of 4-mm 2024 aluminum alloy," Appl. Phys. A **123**, 106 (2017).
[9]M. Gatzen, Z. Tang, F. Vollertsen, M. Mizutani, and S. Katayama, "X-ray investigation of melt flow behavior under magnetic stirring regime in laser beam welding of aluminum," J. Laser Appl. **23**, 032002 (2011).
[10]L. Huang, P. Liu, S. Zhu, X. Hua, and S. Dong, "Experimental research on formation mechanism of porosity in magnetic field assisted laser welding of steel," J. Manuf. Process. **50**, 596–602 (2020).
[11]M. Gatzen, "Influence of low-frequency magnetic fields during laser beam welding of aluminium with filler wire," Phys. Procedia **39**, 59–66 (2012).
[12]L. Li, S. Lou, and C. Wang, "Effect of molten pool and vapor/plasma plume dynamic behavior of laser-induction hybrid welding on weld formation of S690QL steel," Opt. Laser Technol. **150**, 107928 (2022).
[13]A. Schneider, V. Avilov, A. Gumenyuk, and M. Rethmeier, "Laser beam welding of aluminum alloys under the influence of an electromagnetic field," Phys. Procedia **41**, 4–11 (2013).
[14]L. Liang, S. Pang, X. Shao, C. Wang, P. Jiang, and X. Chen, "In situ weak magnetic-assisted thermal stress field reduction effect in laser welding," Metall. Mater. Trans. A **49**, 198–209 (2018).
[15]R. Chen, H. J. Kong, J. H. Luan, A. D. Wang, P. Jiang, and C. T. Liu, "Effect of external applied magnetic field on microstructures and mechanical properties of laser welding joint of medium-Mn nanostructured steel," Mater. Sci. Eng., A **792**, 139787 (2020).
[16]M. Li, J. Xu, Y. Huang, and Y. Rong, "Improving keyhole stability by external magnetic field in full penetration laser welding," J. Miner., Met. Mater. Soc. **70**, 1261–1266 (2018).
[17]C. Hu, F. Yan, Z. Zhu, Y. Xu, J. Tao, and C. Wang, "Effects on microstructural refinement of mechanical properties in steel copper joints laser welded with alternating magnetic field augmentation," Mater. Charact. **175**, 111059 (2021).
[18]L. Xu, X. Tang, R. Zhang, F. Lu, and H. Cui, "Weld bead characteristics for full-penetration laser welding of aluminum alloy under electromagnetic field support," J. Mater. Process. Technol. **288**, 116896 (2021).
[19]C. Hu, C. Wang, X. Ma, Z. Zhu, P. Jiang, and G. Mi, "EBSD study on magnetic field altering crystal texture and grain growth during laser-hybrid welding," Mater. Des. **216**, 110587 (2022).
[20]X. Meng, M. Bachmann, A. Artinov, and M. Rethmeier, "Experimental and numerical assessment of weld pool behavior and final microstructure in wire feed laser beam welding with electromagnetic stirring," J. Manuf. Process. **45**, 408–418 (2019).
[21]F. Yang, X. M. Meng, M. Bachman, A. Artinov, S. N. Putra, and M. Rethmeier, "Numerical analysis of the influence of an auxiliary oscillating magnetic on suppressing the porosity formation in deep penetration laser beam welding of aluminum alloys," in *Proceedings of the 13th International Seminar "Numerical Analysis of Weldabilit," Graz, Austria*, 5 September 2022 (Verlag der Technischen Universität Graz, Graz, Austria, 2022).
[22]Ph. Thévoz, J. L. Desbiolles, and M. Rappaz, "Modeling of equiaxed microstructure formation in casting," Metall. Mater. Trans. A **20**, 311–322 (1989).
[23]P. Jiang, S. Gao, S. Geng, C. Han, and G. Mi, "Multi-physics multi-scale simulation of the solidification process in the molten pool during laser welding of aluminum alloys," Int. J. Heat Mass Transfer **161**, 120316 (2020).
[24]N. Provatas and K. Elder, *Phase-Field Methods in Materials Science and Engineering* (Wiley, Singapore, 2010).
[25]C. Yang, C. S. Wu, and L. Shi, "Phase-field modelling of dynamic recrystallization process during friction stir welding of aluminium alloys," Sci. Technol. Weld. Join. **25**, 345–358 (2020).
[26]J. Chen, Y. Wei, X. Zhan, Q. Gao, D. Zhang, and X. Gao, "Influence of magnetic field orientation on molten pool dynamics during magnet-assisted laser butt welding of thick aluminum alloy plates," Opt. Laser Technol. **104**, 148–158 (2018).
[27]L. Cao, D. Liu, P. Jiang, X. Shao, Q. Zhou, and Y. Wang, "Multi-physics simulation of dendritic growth in magnetic field assisted solidification," Int. J. Heat Mass Transfer **144**, 118673 (2019).
[28]X. Xiao, Y. Fu, X. Ye, M. Cheng, and L. Song, "Analysis of heat transfer and melt flow in conduction, transition, and keyhole modes for CW laser welding," Infrared Phys. Technol. **120**, 103996 (2022).
[29]P. S. Wei, K. C. Chuang, T. DebRoy, and J. S. Ku, "Scaling of spiking and humping in keyhole welding," J. Phys. D: Appl. Phys. **44**, 245501 (2011).
[30]S.-L. Jeng, D.-P. Su, J.-T. Lee, and J.-Y. Huang, "The impact of EMS on the temperature fluctuations, appearance, and microstructure of GTA stainless steel welds," Metals **10**, 118 (2020).